

A multi-resolution technique based on shape optimization for the reconstruction of homogeneous dielectric objects

To cite this article: M Benedetti *et al* 2009 *Inverse Problems* **25** 015009

View the [article online](#) for updates and enhancements.

You may also like

- [Advanced electromagnetic modeling of large-scale high-temperature superconductor systems based on \$H\$ and \$T\$ - \$A\$ formulations](#)
Edgar Berrospe-Juarez, Frederic Trillaud, Víctor M R Zermeño et al.
- [Multi-resolution iterative inversion of real inhomogeneous targets](#)
M Donelli, D Franceschini, A Massa et al.
- [Iterative multi-scale method for estimation of hysteresis losses and current density in large-scale HTS systems](#)
Edgar Berrospe-Juarez, Víctor M R Zermeño, Frederic Trillaud et al.

A multi-resolution technique based on shape optimization for the reconstruction of homogeneous dielectric objects

M Benedetti^{1,2}, D Lesselier², M Lambert² and A Massa¹

¹ Department of Information Engineering and Computer Science, ELEDIA Research Group, University of Trento, Via Sommarive 14, 38050 Trento, Italy

² Département de Recherche en Électromagnétisme, Laboratoire des Signaux et Systèmes, CNRS-SUPELEC Univ. Paris Sud 11, 3 rue Joliot-Curie, 91192 Gif-sur-Yvette Cedex, France

E-mail: manuel.benedetti@disi.unitn.it, lesselier@lss.supelec.fr, lambert@lss.supelec.fr and andrea.massa@ing.unitn.it

Received 19 May 2008, in final form 12 October 2008

Published 24 November 2008

Online at stacks.iop.org/IP/25/015009

Abstract

In the framework of inverse scattering techniques, this paper presents the integration of a multi-resolution technique and the level-set method for qualitative microwave imaging. On the one hand, in order to effectively exploit the limited amount of information collectable from scattering measurements, the iterative multi-scaling approach (IMSA) is employed for enabling a detailed reconstruction only where needed without increasing the number of unknowns. On the other hand, the *a priori* information on the homogeneity of the unknown object is exploited by adopting a shape-based optimization and representing the support of the scatterer via a level-set function. Reliability and effectiveness of the proposed strategy are also assessed by processing both synthetic and experimental scattering data for simple and complex geometries.

(Some figures in this article are in colour only in the electronic version)

1. Introduction

The non-invasive reconstruction of the position and shape of unknown targets is a topic of great interest in many applications, such as non-destructive evaluation and testing (NDE/NDT) for industrial monitoring and sub-surface sensing [1]. In this framework, many methodologies have been proposed based on x-rays [2], ultrasonics [3] and eddy currents [4]. Furthermore, microwave imaging has been recognized as a suitable methodology since [1, 5]: (a) electromagnetic fields at microwave frequencies can penetrate non-ideal conductor materials; (b) the field scattered by the target is representative of its inner structure and not

only of its boundary; (c) microwaves show a high sensibility to the water content of the structure under test; (d) microwave sensors can be employed without mechanical contacts with the specimen. In addition, compared to x-ray and magnetic resonance, microwave-based approaches minimize (or avoid) collateral effects in the specimen under test. Therefore, they can be safely employed in biomedical imaging.

A further advance in microwave non-invasive inspection is represented by inverse scattering approaches aimed at reconstructing a complete image of the region under test. Unfortunately, the underlying mathematical model is characterized by several drawbacks preventing their massive employment in NDE/NDT applications. In particular, inverse scattering problems are intrinsically ill-posed [6] as well as nonlinear [7].

Since the ill-posedness is strongly related to the amount of collectable information and usually the number of independent data is lower than the dimension of the solution space, multi-view/multi-illumination systems are generally adopted. However, it is well known that the collectable information is an upper-bounded quantity [8–10]. Consequently, it is necessary to effectively exploit the overall information contained in the scattered field samples for achieving a satisfactory reconstruction.

Toward this end, multi-resolution strategies have been recently proposed. The idea is that of using an enhanced spatial resolution only in those regions where the unknown scatterers are found to be located. Accordingly, Miller *et al* [11] proposed a statistically-based method for determining the optimal resolution level, while Baussard *et al* [12] developed a strategy based on spline pyramids for sub-surface imaging problems. As for an example concerned with qualitative microwave imaging, Li *et al* [13] implemented a multi-scale technique based on the linear sampling method (LSM) to effectively reconstruct the contour of the scatterers. Unlike [11–13], the iterative multi-scale approach (IMSA) developed by Caorsi *et al* [14] performs a multi-step, multi-resolution inversion process in which the ratio between unknowns and data is kept suitably low and constant at each step of the inversion procedure, thus reducing the risk of occurrence of local minima [9] in the arising optimization problem.

On the other hand, the lack of information affecting the inverse problem has been addressed through the exploitation of the *a priori* knowledge (when available) on the scenario under test by means of an effective representation of the unknowns. As far as many NDE/NDT applications are concerned, the unknown defect is characterized by known electromagnetic properties (i.e., dielectric permittivity and conductivity) and it lies within a known host region. Under these assumptions, the imaging problem reduces to a shape optimization problem aimed at the search of location and boundary contours of the defect. Parametric techniques aimed at representing the unknown object in terms of descriptive parameters of reference shapes [15, 16] and more sophisticated approaches such as evolutionary-controlled spline curves [17, 18], shape gradients [19–21] or level sets [22–30] have then been proposed. As far as level-set-based methods are concerned, the homogeneous object is defined as the zero level of a continuous function and, unlike pixel-based or parametric-based strategies, such a description enables one to represent complex shapes in a simple way.

In order to exploit both the available *a priori* knowledge on the scenario under test (e.g., the homogeneity of the scatterer) and the information content from the scattering measurements, this paper proposes the integration of the iterative multi-scaling strategy (IMSA) [14] and the level-set (LS) representation [23].

The paper is structured as follows. The integration between IMSA and LS is detailed in section 2 dealing with a two-dimensional geometry. In section 3, numerical testing and experimental validation are presented, a comparison with the standard LS implementation being made. Finally, some conclusions are drawn (section 4).

2. Mathematical formulation

Let us consider a cylindrical homogeneous non-magnetic object with relative permittivity ϵ_C and conductivity σ_C that occupies a region Υ belonging to an investigation domain D_I . Such a scatterer is probed by a set of V transverse-magnetic (TM) plane waves, with an electric field directed along the axis of the cylindrical geometry, namely $\underline{\zeta}^v(\underline{r}) = \zeta^v(\underline{r})\hat{z}$ ($v = 1, \dots, V$), $\underline{r} = (x, y)$. The scattered field, $\underline{\xi}^v(\underline{r}) = \xi^v(\underline{r})\hat{z}$, is collected at $M(v)$, $v = 1, \dots, V$, measurement points \underline{r}_m distributed in the observation domain D_O .

In order to electromagnetically describe the investigation domain D_I , let us define the contrast function $\tau(\underline{r})$ given by

$$\tau(\underline{r}) = \begin{cases} \tau_C & \underline{r} \in \Upsilon \\ 0 & \text{otherwise,} \end{cases} \quad (1)$$

where $\tau_C = (\epsilon_C - 1) - j\frac{\sigma_C}{2\pi f \epsilon_0}$, f being the frequency of operation (the time dependence $e^{j2\pi f t}$ being implied).

The scattering problem is described by the well-known Lippmann–Schwinger integral equations

$$\xi^v(\underline{r}_m) = \left(\frac{2\pi}{\lambda}\right)^2 \int_{D_I} \tau(\underline{r}') E^v(\underline{r}') G_{2D}(\underline{r}_m, \underline{r}') d\underline{r}', \quad \underline{r}_m \in D_O \quad (2)$$

$$\zeta^v(\underline{r}) = E^v(\underline{r}) - \left(\frac{2\pi}{\lambda}\right)^2 \int_{D_I} \tau(\underline{r}') E^v(\underline{r}') G_{2D}(\underline{r}, \underline{r}') d\underline{r}', \quad \underline{r} \in D_I \quad (3)$$

where λ is the background wavelength, E^v is the total electric field, and $G_{2D}(\underline{r}, \underline{r}') = -\frac{j}{4} H_0^{(2)}\left(\frac{2\pi}{\lambda} \|\underline{r} - \underline{r}'\|\right)$ is the free-space two-dimensional Green's function, $H_0^{(2)}$ being the second-kind, zeroth-order Hankel function.

In order to retrieve the unknown position and shape of the target Υ by step-by-step enhancing the spatial resolution only in that region, called region-of-interest (RoI), $R \in D_I$, where the scatterer is located [14], the following iterative procedure of S_{\max} steps is carried out.

With reference to figure 1(a) and to the block diagram displayed in figure 2, at the first step ($s = 1$, s being the step number) a trial shape $\Upsilon_s = \Upsilon_1$, belonging to D_I , is chosen and the region of interest R_s [$R_{s=1} = D_I$] is partitioned into N_{IMSA} equal square sub-domains, where N_{IMSA} depends on the degrees of freedom of the problem at hand and it is computed according to the guidelines suggested in [9].

In addition, the level-set function ϕ_s is initialized by means of a signed distance function defined as follows [23, 25]:

$$\phi_s(\underline{r}) = \begin{cases} -\min_{b=1, \dots, B_s} \|\underline{r} - \underline{r}_b\| & \text{if } \tau(\underline{r}) = \tau_C \\ \min_{b=1, \dots, B_s} \|\underline{r} - \underline{r}_b\| & \text{if } \tau(\underline{r}) = 0 \end{cases} \quad (4)$$

where $\underline{r}_b = (x_b, y_b)$ is the b th border-cell ($b = 1, \dots, B_s$) of $\Upsilon_{s=1}$.

Then, at each step s of the process ($s = 1, \dots, S_{\max}$), the following optimization procedure is repeated (figure 2):

- *Problem unknown representation.* The contrast function is represented in terms of the level-set function as follows:

$$\tilde{\tau}_{k_s}(\underline{r}) = \sum_{i=1}^s \sum_{n_i=1}^{N_{\text{IMSA}}} \tau_{k_i} \mathcal{B}(\underline{r}_{n_i}) \quad \underline{r} \in D_I, \quad (5)$$

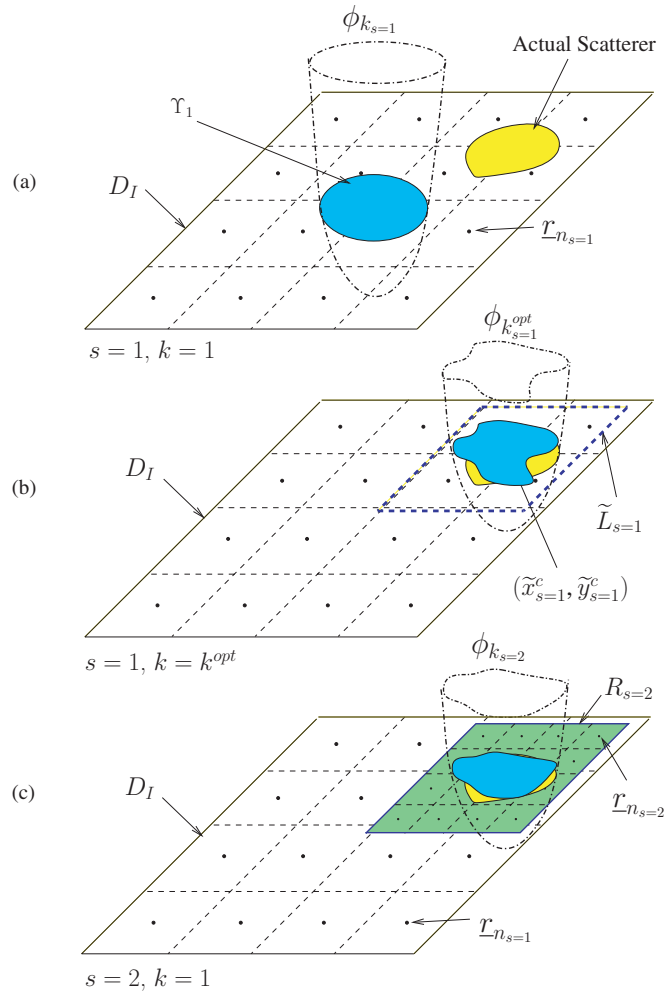


Figure 1. Graphical representation of the IMSA-LS zooming procedure. (a) First step ($k = 1$): the investigation domain is discretized in N sub-domains and a coarse solution is looked for. (b) First step ($k = k^{opt}$): the region of interest that contains the first estimate of the object is defined. (c) Second step ($k = 1$): an enhanced resolution level is used only inside the region of interest.

where the index k_s indicates the k th iteration at the s th step [$k_s = 1, \dots, k_s^{opt}$], $\mathcal{B}(\underline{r}_{n_i})$ is a rectangular basis function whose support is the n th sub-domain at the i th resolution level [$n_i = 1, \dots, N_{IMSA}, i = 1, \dots, s$], and the coefficient τ_{k_i} is given by

$$\tau_{k_i} = \begin{cases} \tau_C & \text{if } \Psi_{k_i}(\underline{r}_{n_i}) \leq 0 \\ 0 & \text{otherwise} \end{cases} \quad (6)$$

letting

$$\Psi_{k_i}(\underline{r}_{n_i}) = \begin{cases} \phi_{k_i}(\underline{r}_{n_i}) & \text{if } i = s \\ \phi_{k_i^{opt}}(\underline{r}_{n_i}) & \text{if } (i < s) \text{ and } (\underline{r}_{n_i} \in R_i) \end{cases} \quad (7)$$

with $i = 1, \dots, s$ as in (5).

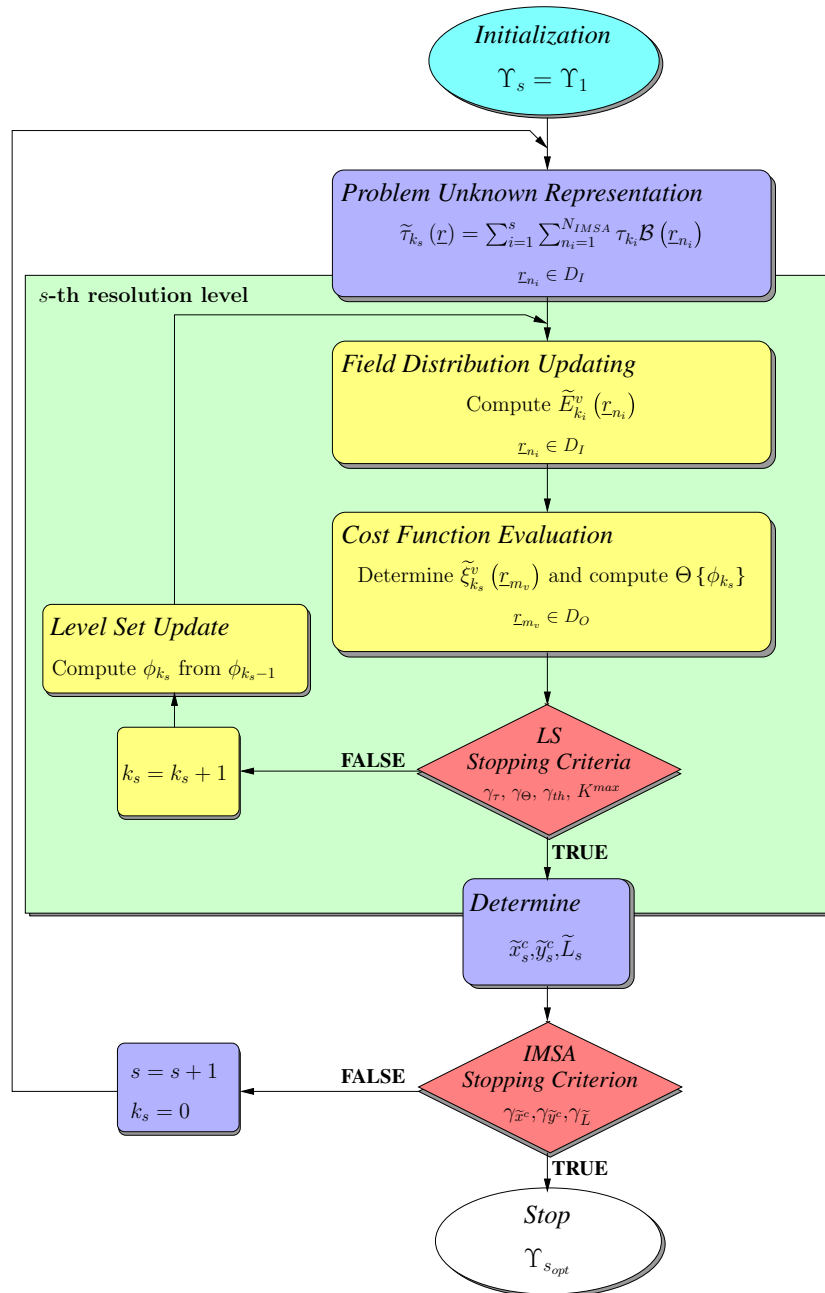


Figure 2. Block diagram description of the IMSA-LS zooming procedure.

- *Field distribution updating.* Once $\tilde{\tau}_{k_s}(\underline{r})$ has been estimated, the electric field $E_{k_s}^v(\underline{r})$ is numerically computed according to a point-matching version of the Method of Moments (MoM) [31] as

$$\tilde{E}_{k_i}^v(\underline{r}_{n_i}) = \sum_{p_i=1}^{N_{\text{IMSA}}} \zeta^v(\underline{r}_{p_i}) [1 - \tilde{\tau}_{k_i}(\underline{r}_{p_i}) G_{2D}(\underline{r}_{n_i}, \underline{r}_{p_i})]^{-1}, \quad \underline{r}_{n_i}, \underline{r}_{p_i} \in D_I \quad (8)$$

$$n_i = 1, \dots, N_{\text{IMSA}}.$$

- *Cost function evaluation.* Starting from the total electric field distribution (8), the reconstructed scattered field $\tilde{\xi}_{k_s}^v(\underline{r}_m)$ at the m th measurement point, $m = 1, \dots, M(v)$, is updated by solving the following equation:

$$\tilde{\xi}_{k_s}^v(\underline{r}_m) = \sum_{i=1}^s \sum_{n_i=1}^{N_{\text{IMSA}}} \tilde{\tau}_{k_i}(\underline{r}_{n_i}) \tilde{E}_{k_i}^v(\underline{r}_{n_i}) G_{2D}(\underline{r}_m, \underline{r}_{n_i}) \quad (9)$$

and the fit between measured and reconstructed data is evaluated by the multi-resolution cost function Θ defined as

$$\Theta\{\phi_{k_s}\} = \frac{\sum_{v=1}^V \sum_{m=1}^{M(v)} |\tilde{\xi}_{k_s}^v(\underline{r}_m) - \xi_{k_s}^v(\underline{r}_m)|^2}{\sum_{v=1}^V \sum_{m=1}^{M(v)} |\xi_{k_s}^v(\underline{r}_m)|^2}. \quad (10)$$

- *Minimization stopping.* The iterative process stops (i.e., $k_s^{\text{opt}} = k_s$ and $\tilde{\tau}_s^{\text{opt}} = \tilde{\tau}_{k_s}$) when: (a) a set of conditions on the stability of the reconstruction holds true or (b) when the maximum number of iterations is reached [$k_s = K_{\text{max}}$] or (c) when the value of the cost function is smaller than a fixed threshold γ_{th} . As far as the stability of the reconstruction is concerned (condition (a)), the first corresponding stopping criterion is satisfied when, for a fixed number of iterations, K_τ , the maximum number of pixels which vary their value is smaller than a user-defined threshold γ_τ according to the relationship

$$\max_{j=1, \dots, K_\tau} \left\{ \sum_{n_s=1}^{N_{\text{IMSA}}} \frac{|\tilde{\tau}_{k_s}(\underline{r}_{n_s}) - \tilde{\tau}_{k_s-j}(\underline{r}_{n_s})|}{\tau_C} \right\} < \gamma_\tau \cdot N_{\text{IMSA}}. \quad (11)$$

The second criterion, about the stability of the reconstruction, is satisfied when the cost function becomes stationary within a window of K_Θ iterations as follows:

$$\frac{1}{K_\Theta} \sum_{j=1}^{K_\Theta} \frac{\Theta\{\phi_{k_s}\} - \Theta\{\phi_{k_s-j}\}}{\Theta\{\phi_{k_s}\}} < \gamma_\Theta. \quad (12)$$

K_Θ being a fixed number of iterations and γ_Θ being user-defined thresholds. When the iterative process stops, the solution $\tilde{\tau}_s^{\text{opt}}$ at the s th step is selected as that represented by the ‘best’ level-set function ϕ_s^{opt} defined as

$$\phi_s^{\text{opt}} = \arg[\min_{h=1, \dots, k_s^{\text{opt}}} (\Theta\{\phi_h\})]. \quad (13)$$

- *Iteration update.* The iteration index is updated [$k_s \rightarrow k_s + 1$].
- *Level-set update.* The level set is updated according to the following Hamilton–Jacobi relationship:

$$\phi_{k_s}(\underline{r}_{n_s}) = \phi_{k_s-1}(\underline{r}_{n_s}) - \Delta t_s \mathcal{V}_{k_s-1}(\underline{r}_{n_s}) \mathcal{H}\{\phi_{k_s-1}(\underline{r}_{n_s})\}, \quad (14)$$

where $\mathcal{H}\{\cdot\}$ is the Hamiltonian operator [32, 33] given as

$$\mathcal{H}^2\{\phi_{k_s}(\underline{r}_{n_s})\} = \begin{cases} \max^2\{\mathcal{D}_{k_s}^{x-}; 0\} + \min^2\{\mathcal{D}_{k_s}^{x+}; 0\} + \max^2\{\mathcal{D}_{k_s}^{y-}; 0\} + \min^2\{\mathcal{D}_{k_s}^{y+}; 0\} \\ \text{if } \mathcal{V}_{k(s)}(\underline{r}_{n(s)}) \geq 0 \\ \min^2\{\mathcal{D}_{k_s}^{x-}; 0\} + \max^2\{\mathcal{D}_{k_s}^{x+}; 0\} + \min^2\{\mathcal{D}_{k_s}^{y-}; 0\} + \max^2\{\mathcal{D}_{k_s}^{y+}; 0\} \\ \text{otherwise} \end{cases} \quad (15)$$

and

$$\mathcal{D}_{k_s}^{x\pm} = \frac{\pm\phi_{k_s}(x_{n_s\pm 1}, y_{n_s}) \mp \phi_{k_s}(x_{n_s}, y_{n_s})}{l_s},$$

$$\mathcal{D}_{k_s}^{y\pm} = \frac{\pm\phi_{k_s}(x_{n_s}, y_{n_s\pm 1}) \mp \phi_{k_s}(x_{n_s}, y_{n_s})}{l_s}.$$

Δt_s is the time-step chosen as $\Delta t_s = \Delta t_1 \frac{l_s}{l_1}$ with Δt_1 to be set heuristically according to the literature [23], l_s being the cell side at the s th resolution level. \mathcal{V}_{k_s} is the velocity function computed following the guidelines suggested in [23] by solving the adjoint problem of (8) in order to determine the adjoint field $\mathcal{F}_{k_s}^v$. Accordingly,

$$\mathcal{V}_{k_s}(\underline{r}_{n_s}) = -\text{Re} \left\{ \frac{\sum_{v=1}^V \tau_C E_{k_s}^v(\underline{r}_{n_s}) \mathcal{F}_{k_s}^v(\underline{r}_{n_s})}{\sum_{v=1}^V \sum_{m=1}^{M(v)} |\xi_{k_s}^v(\underline{r}_m)|^2} \right\}, \quad n_s = 1, \dots, N_{\text{IMSA}} \quad (16)$$

where Re stands for the real part.

When the s th minimization process terminates, the contrast function is updated [$\tilde{\tau}_s^{\text{opt}}(\underline{r}) = \tilde{\tau}_{k_{s-1}}^{\text{opt}}(\underline{r})$, $\underline{r} \in D_I$ (5)] as well as the RoI [$R_s \rightarrow R_{s-1}$]. To do so, the following operations are carried out:

- *Computation of the barycenter of the RoI.* The center of R_s of coordinates $(\tilde{x}_s^c, \tilde{y}_s^c)$ is determined by computing the center of mass of the reconstructed shapes as follows [14] (figure 1(b)):

$$\tilde{x}_s^c = \frac{\int_{D_I} x \tilde{\tau}_s^{\text{opt}}(\underline{r}) \mathcal{B}(\underline{r}) \, dx \, dy}{\int_{D_I} \tilde{\tau}_s^{\text{opt}}(\underline{r}) \mathcal{B}(\underline{r}) \, dx \, dy} \quad (17)$$

$$\tilde{y}_s^c = \frac{\int_{D_I} y \tilde{\tau}_s^{\text{opt}}(\underline{r}) \mathcal{B}(\underline{r}) \, dx \, dy}{\int_{D_I} \tilde{\tau}_s^{\text{opt}}(\underline{r}) \mathcal{B}(\underline{r}) \, dx \, dy}; \quad (18)$$

- *Estimation of the Size of the RoI.* The side L_s of R_s is computed by evaluating the maximum of the distance $\delta_c(\underline{r}) = \sqrt{(x - \tilde{x}_s^c)^2 + (y - \tilde{y}_s^c)^2}$ in order to enclose the scatterer, namely

$$\tilde{L}_s = \max_{\underline{r}} \left\{ 2 \times \frac{\tilde{\tau}_s^{\text{opt}}(\underline{r})}{\tau_C} \delta_c(\underline{r}) \right\}. \quad (19)$$

Once the RoI has been identified, the level of resolution is enhanced [$k_s \rightarrow k_{s-1}$] only in this region by discretizing R_s into N_{IMSA} sub-domains (figure 1(c)) and by repeating the minimization process until the synthetic zoom becomes stationary ($s = s_{\text{opt}}$), i.e.,

$$\left\{ \frac{|Q_{s-1} - Q_s|}{|Q_{s-1}|} \times 100 \right\} < \gamma_Q, \quad Q = \tilde{x}^c, \tilde{y}^c, \tilde{L} \quad (20)$$

γ_Q being a threshold set as in [14], or until a maximum number of steps ($s_{\text{opt}} = S_{\text{max}}$) is reached.

At the end of the multi-step process ($s = s_{\text{opt}}$), the problem solution is obtained as $\tilde{\tau}^{\text{opt}}(\underline{r}_{n_i}) = \tilde{\tau}_s^{\text{opt}}(\underline{r}_{n_i})$, $n_i = 1, \dots, N_{\text{IMSA}}$, $i = 1, \dots, s_{\text{opt}}$.

3. Numerical validation

In order to assess the effectiveness of the IMSA-LS approach, a selected set of representative results concerned with both synthetic and experimental data is presented herein. The performances achieved are evaluated by means of the following error figures:

- *Localization error* δ

$$\delta|_p = \frac{\sqrt{(\tilde{x}_s^c|_p - x^c|_p)^2 - (\tilde{y}_s^c|_p - y^c|_p)^2}}{\lambda} \times 100, \quad (21)$$

where $r_c|_p = (x^c|_p, y^c|_p)$ is the center of the p th true scatterer, $p = 1, \dots, P$, P being the number of objects. The average localization error $\langle \delta \rangle$ is defined as

$$\langle \delta \rangle = \frac{1}{P} \sum_{p=1}^P \delta|_p. \quad (22)$$

- *Area estimation error* Δ

$$\Delta = \left[\sum_{i=1}^I \frac{1}{N_{\text{IMSA}}} \sum_{n_i=1}^{N_{\text{IMSA}}} \mathcal{N}_{n_i} \right] \times 100 \quad (23)$$

where \mathcal{N}_{n_i} is equal to 1 if $\tilde{\tau}^{\text{opt}}(r_{n_i}) = \tau(r_{n_i})$ and 0 otherwise.

As far as the numerical experiments are concerned, the reconstructions have been performed by blurring the scattering data with an additive Gaussian noise characterized by a signal-to-noise ratio (SNR)

$$\text{SNR} = 10 \log \frac{\sum_{v=1}^V \sum_{m=1}^{M(v)} |\xi^v(r_m)|^2}{\sum_{v=1}^V \sum_{m=1}^{M(v)} |\mu^{v,m}|^2} \quad (24)$$

$\mu^{v,m}$ being a complex Gaussian random variable with zero mean value.

3.1. Synthetic data—circular cylinder

3.1.1. Preliminary validation. In the first experiment, a lossless circular off-centered scatterer of known permittivity $\epsilon_C = 1.8$ and radius $\rho = \lambda/4$ is located in a square investigation domain of side $L_D = \lambda$ [23]. $V = 10$ TM plane waves are impinging from the directions $\theta_v = 2\pi(v-1)/V$, $v = 1, \dots, V$, and the scattering measurements are collected at $M = 10$ receivers uniformly distributed on a circle of radius $\rho_O = \lambda$.

As far as the initialization of the IMSA-LS algorithm is concerned, the initial trial object Υ_1 is a disk with radius $\lambda/4$ and centered in D_I . The initial value of the time step is set to $\Delta t_1 = 10^{-2}$ as in [23]. The RoI is discretized in $N_{\text{IMSA}} = 15 \times 15$ sub-domains at each step of the iterative multi-resolution process. Concerning the stopping criteria, the following configuration of parameters has been selected according to a preliminary calibration dealing with simple known scatterers and noiseless data: $S_{\text{max}} = 4$ (maximum number of steps), $\gamma^{\tilde{x}^c} = \gamma^{\tilde{y}^c} = 0.01$ and $\gamma^{\tilde{L}} = 0.05$ (multi-step process thresholds), $K_{\text{max}} = 500$ (maximum number of optimization iterations), $\gamma_{\ominus} = 0.2$ and $\gamma_{\tau} = 0.02$ (optimization thresholds), $K_{\ominus} = K_{\tau} = 0.15 K_{\text{max}}$ (stability counters), and $\gamma_{\text{th}} = 10^{-5}$ (threshold on the cost function).

Figure 3 shows samples of reconstructions with the IMSA-LS. At the first step (figure 3(a), $s = 1$), the scatterer is correctly located, but its shape is only roughly estimated. Thanks to the multi-resolution representation, the qualitative imaging of the scatterer is

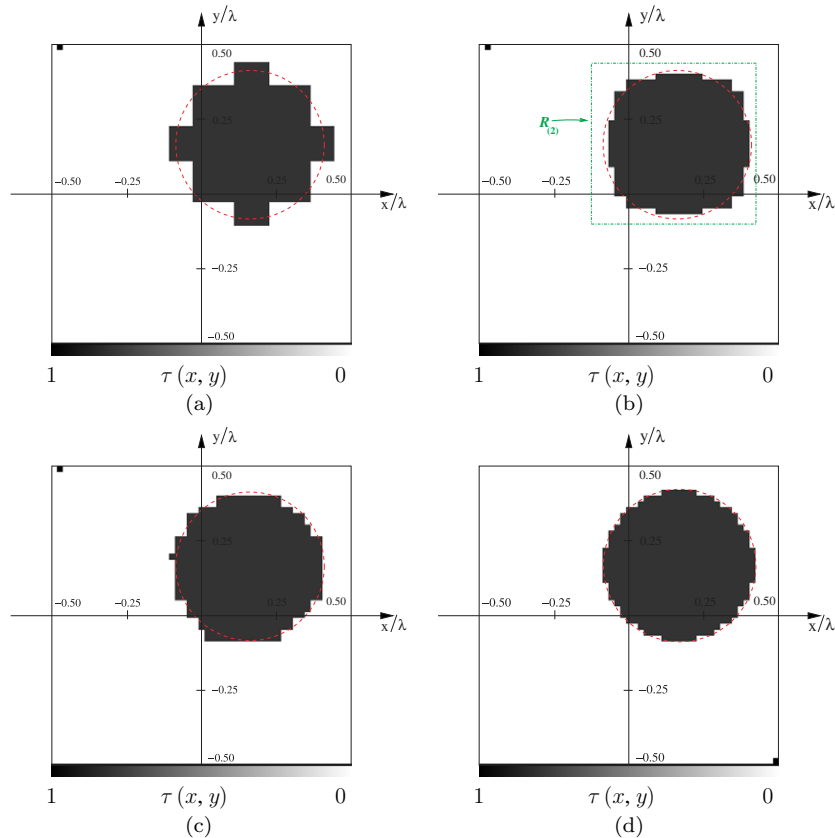


Figure 3. Numerical data. Circular cylinder ($\epsilon_C = 1.8$, $L_D = \lambda$, *noiseless case*). Reconstructions with IMSA-LS at (a) $s = 1$ and (b) $s = s_{\text{opt}} = 2$, (c) Bare-LS. Optimal inversion (d).

Table 1. Numerical Data. Circular cylinder ($\epsilon_C = 1.8$, *noiseless case*). Error figures.

	IMSA-LS		Bare-LS
	$s = 1$	$s = 2$	
δ	6.58×10^{-6}	2.19×10^{-6}	5.21×10^{-1}
Δ	2.36	0.48	0.64

improved in the next step (figure 3(b), $s = s_{\text{opt}} = 2$) as confirmed by the error indexes in table 1. For comparison purposes, the profile retrieved by the single-resolution method [23] (indicated in the following as Bare-LS), when D_I has been discretized in $N_{\text{Bare}} = 31 \times 31$ equal sub-domains, is shown (figure 3(c)). In general, the discretization of the Bare-LS has been chosen in order to achieve in the whole investigation domain a reconstruction with the same level of spatial resolution obtained by the IMSA-LS in the RoI at $s = s_{\text{opt}}$.

Although the final reconstructions (figures 3(b), (c)) achieved by the two approaches are similar and quite close to the true scatterer sampled at the spatial resolution of Bare-LS (figure 3(d)) and IMSA-LS (figure 3(b)), the IMSA-LS more faithfully retrieves the symmetry of the actual object, even though the reconstruction error appears to be larger than that of the

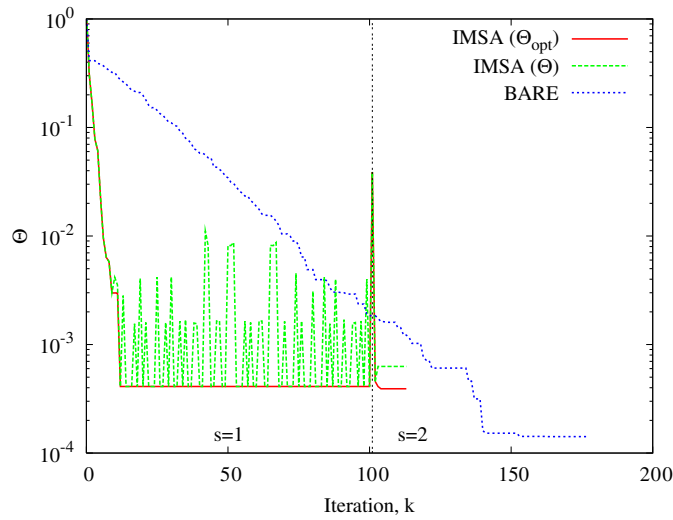


Figure 4. Numerical data. Circular cylinder ($\epsilon_C = 1.8$, $L_D = \lambda$, noiseless case). Behavior of the cost function.

Bare-LS (figure 4). During the iterative procedure, the cost function $\Theta_{\text{opt}} = \Theta\{\phi_s^{\text{opt}}\}$ is initially characterized by a monotonically decreasing behavior. Then, $\Theta_{\text{opt}|_{\text{IMSA}}}$ becomes stationary until the stopping criterion defined by relationships (11) and (12) is satisfied (figure 4, $s = 1$). Then, after the update of the field distribution inducing the error spike when $s = s_{\text{opt}} = 2$ and $k_s = 1$, $\Theta_{\text{opt}|_{\text{IMSA}}}$ settles to a value of 6.28×10^{-4} which is of the order of the Bare-LS error ($\Theta_{\text{opt}|_{\text{Bare}}} = 1.42 \times 10^{-4}$). Such a slight difference between $\Theta_{\text{opt}|_{\text{IMSA}}}$ and $\Theta_{\text{opt}|_{\text{Bare}}}$ depends on the different discretization (i.e., the basis functions $\mathcal{B}(r_{n(i=2)}), n(i) = 1, \dots, N_{\text{IMSA}}$ are not the same as those of Bare-LS), but it does not affect the reconstruction in terms of both localization and area estimation, since $\delta|_{\text{IMSA-LS}} < \delta|_{\text{Bare-LS}}$ and $\Delta|_{\text{IMSA-LS}} < \Delta|_{\text{Bare-LS}}$ (table 1).

Figure 4 also shows that the multi-step multi-resolution strategy is characterized by a lower computational burden because of the smaller number of iterations for reaching the convergence (figure 4, $k_{\text{tot}|_{\text{IMSA}}} = 125$ versus $k_{\text{tot}|_{\text{Bare}}} = 177$, k_{tot} being the total number of iterations defined as $k_{\text{tot}} = \sum_{s=1}^{s_{\text{opt}}} k_s^{\text{opt}}$ for the IMSA-LS), and especially to the reduced number of floating-point operations. As a matter of fact, since the complexity of the LS-based algorithms is of the order of $\mathcal{O}(2 \times \eta^3)$, $\eta = N_{\text{IMSA}}, N_{\text{Bare}}$ (i.e., the solution of two direct problems is necessary for computing an estimate of the scattered field and for updating the velocity vector), the computational cost of the IMSA-LS at each iteration is two orders in magnitude smaller than that of the Bare-LS.

3.1.2. Noisy data. As for the stability of the proposed approach, figure 5 shows the reconstructions with the IMSA-LS (figures 5(a), (c), (e)) compared to those of the Bare-LS (figures 5(b), (d), (f)) with different levels of additive noise on the scattered data (SNR = 20 dB (top); SNR = 10 dB (middle); SNR = 5 dB (bottom)). As expected, when the SNR decreases, the performances worsen. However, as outlined by the behavior of the error figures in table 2, blurred data and/or noisy conditions affect more evidently the Bare implementation than the multi-resolution approach. For completeness, the behavior of $\Theta_{\text{opt}|_{\text{IMSA}}}$ versus the iteration index is reported in figure 6 for different levels of SNR. As it

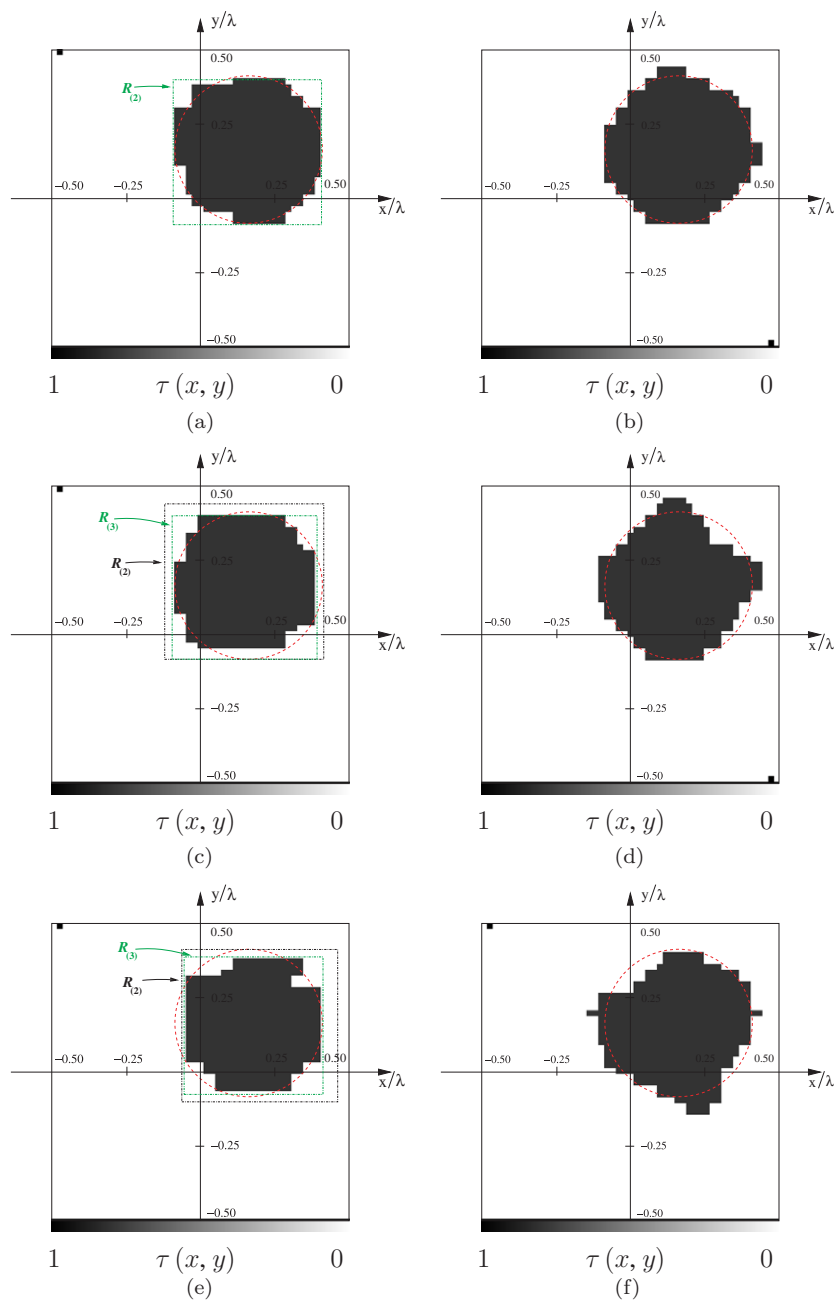


Figure 5. Circular cylinder ($\epsilon_C = 1.8$, $L_D = \lambda$, *noisy case*). Reconstructions with IMSA-LS (left column) and Bare-LS (right column) for different values of SNR (SNR = 20 dB (top), SNR = 10 dB (middle), SNR = 5 dB (bottom)).

can be noticed, the value of the error at the end of the iterative procedure decreases as the SNR increases.

In the second experiment, the same circular scatterer, but centered at a different position within a larger investigation square of side $L_D = 2\lambda$ ($\rho_O = 2\lambda$), has been reconstructed.

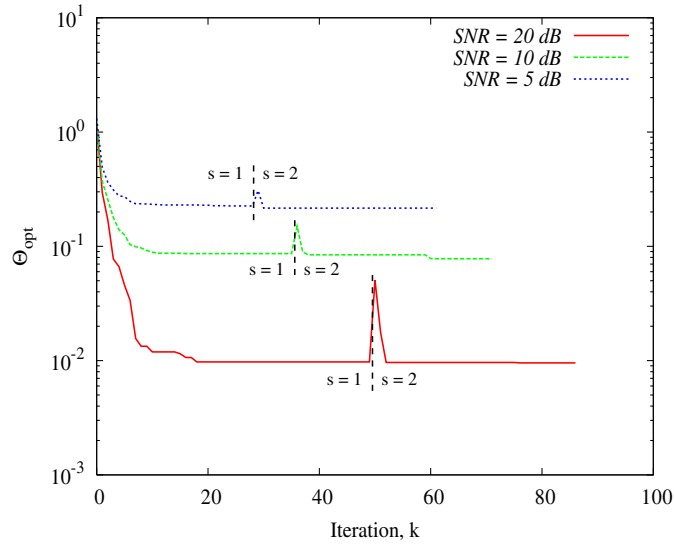


Figure 6. Numerical data. Circular cylinder ($\epsilon_C = 1.8$, $L_D = \lambda$). Behavior of the cost function versus the noise level.

Table 2. Numerical data. Circular cylinder ($\epsilon_C = 1.8$, *noisy case*). Values of the error indexes for different values of SNR.

	SNR = 20 dB		SNR = 10 dB		SNR = 5 dB	
	IMSA-LS	Bare-LS	IMSA-LS	Bare-LS	IMSA-LS	Bare-LS
δ	5.91×10^{-1}	2.72	2.28	2.45	6.78×10^{-1}	1.63
Δ	0.98	1.28	1.07	1.80	1.50	2.07

According to [9], $M = 20$; $v = 1, \dots, V$ receivers and $V = 20$ views are considered and D_I is discretized in $N_{\text{IMSA}} = 13 \times 13$ pixels.

Figure 7(a) shows the reconstruction obtained at the convergence ($s_{\text{opt}} = 3$) by IMSA-LS when SNR = 5 dB. The result reached by the Bare-LS ($N_{\text{BARE}} = 47 \times 47$) is reported in figure 7(b) as well. As it can be noticed, the multi-resolution inversion is characterized by a better estimation of the object center and shape as confirmed by the values of δ and Δ ($\delta_{\text{IMSA-LS}} = 0.59$ versus $\delta_{\text{Bare-LS}} = 2.72$ and $\Delta_{\text{IMSA-LS}} = 0.48$ versus $\Delta_{\text{Bare-LS}} = 0.64$). As for the computational load, the same conclusions from previous experiments hold true.

3.2. Synthetic data—rectangular scatterer

The second test case deals with a more complex scattering configuration. A rectangular off-centered scatterer ($L = 0.27\lambda$ and $W = 0.13\lambda$) characterized by a dielectric permittivity $\epsilon_C = 1.8$ is located within an investigation domain of $L_D = 3\lambda$ as indicated by the red dashed line in figure 8. In such a case, the imaging setup is made up of $V = 30$ sources and $M = 30$ measurement points for each view v [9]. D_I is partitioned into $N_{\text{IMSA}} = 19 \times 19$ sub-domains (while $N_{\text{Bare}} = 33 \times 33$) and Δt_1 is set to 0.06.

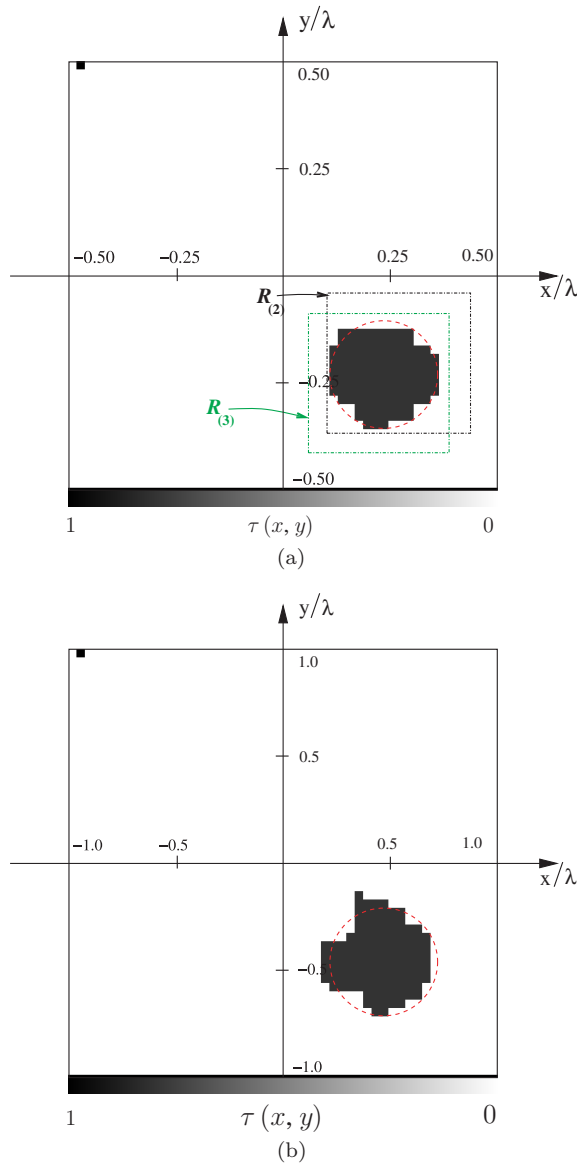


Figure 7. Numerical data. Circular cylinder ($\epsilon_C = 1.8$, $L_D = 2\lambda$, SNR = 5 dB). Reconstructions with (a) IMSA-LS and (b) Bare-LS.

3.2.1. Validation of the stopping criteria. Before discussing the reconstruction capabilities, let us show a result concerned with the behavior of the proposed approach when varying the user-defined thresholds (γ_Θ , γ_τ , $\gamma_{\tilde{x}^c}$, $\gamma_{\tilde{y}^c}$, $\gamma_{\tilde{z}}$) of the stopping criteria. Figure 8 displays the reconstructions achieved by using the sets of parameters given in table 3 (Γ_1 , figure 8(a); Γ_2 , figure 8(b); Γ_3 , figure 8(c); Γ_4 , figure 8(d)) while the behaviors of the cost function are depicted in figure 9. As it can be noticed, the total number of iterations k_{tot} increases as the values of the thresholds γ_Θ and γ_τ decrease. However, in spite of a larger k_{tot} , using lower threshold

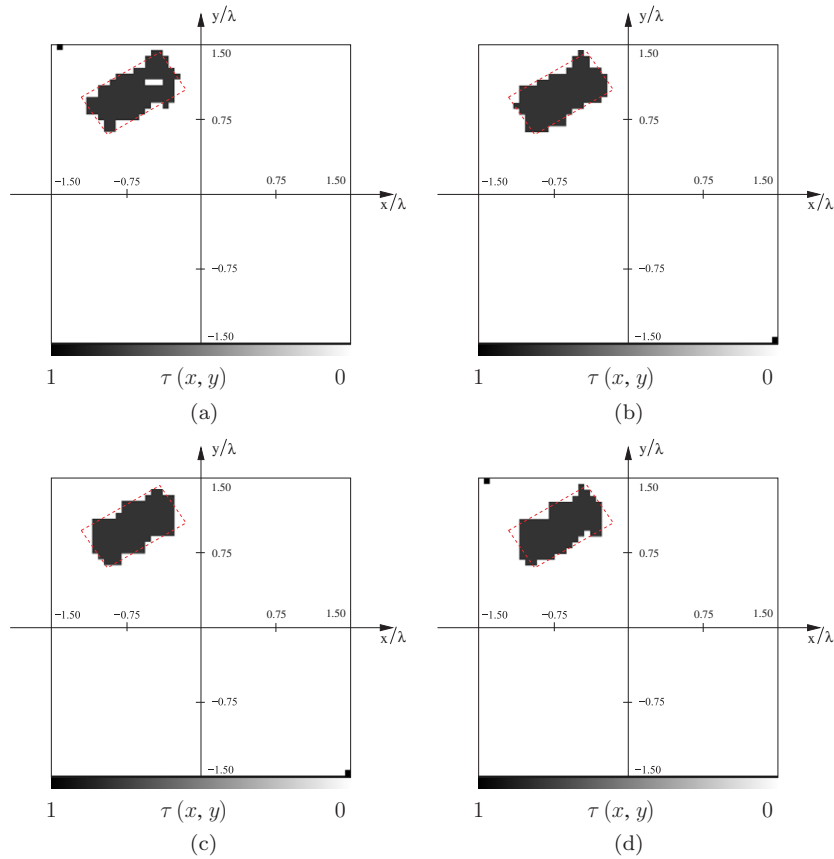


Figure 8. Numerical data. Rectangular cylinder ($\epsilon_C = 1.8, L_D = 3\lambda$, noiseless case). Reconstructions with IMSA-LS for the different settings of table 3 ((a) Γ_1 , (b) Γ_2 , (c) Γ_3 , (d) Γ_4).

Table 3. Numerical data. Rectangular cylinder ($\epsilon_C = 1.8, L_D = 3\lambda$, noiseless case). Different settings for the parameters of the stopping criteria.

Set of parameters	γ_Θ	γ_τ	$\gamma_{\tilde{\kappa}^c}, \gamma_{\tilde{\gamma}^c}$	$\gamma_{\tilde{L}}$
Γ_1	0.5	0.05	0.01	0.05
Γ_2	0.2	0.02	0.01	0.05
Γ_3	0.2	0.02	0.1	0.5
Γ_4	0.02	0.002	0.01	0.05

values does not provide better results, as shown by the comparison between settings Γ_2 and Γ_4 (figures 8(b)–(d), and figure 9). The sets of parameters characterized by $\gamma_\Theta = 0.2$ and $\gamma_\tau = 0.02$ provide a good trade-off between the arising computational burden and the quality of the reconstructions. As far as the stopping criterion of the multi-resolution procedure is concerned, figure 9 also shows two different behaviors of the cost function when using Γ_2 and Γ_3 (letting $\gamma_\Theta = 0.2$ and $\gamma_\tau = 0.02$). In particular, the proposed approach stops at $s_{\text{opt}} = 3$, instead of $s_{\text{opt}} = 4$, when increasing by a degree of magnitude the values of $\gamma_{\tilde{\kappa}^c}, \gamma_{\tilde{\gamma}^c}$ and $\gamma_{\tilde{L}}$.

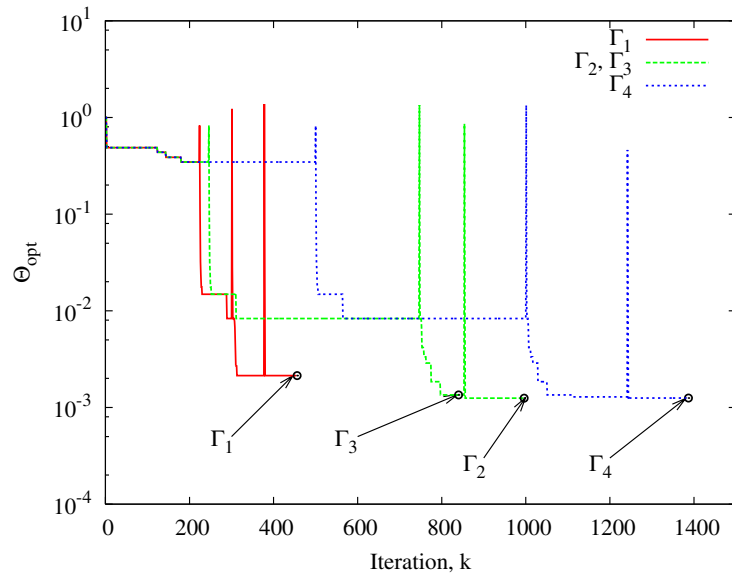


Figure 9. Numerical data. Rectangular cylinder ($\epsilon_C = 1.8$, $L_D = 3\lambda$, noiseless case). Behavior of the cost function of IMSA-LS for the different settings of table 3.

Table 4. Numerical data. Rectangular cylinder ($\epsilon_C = 1.8$, $L_D = 3\lambda$, noisy case). Computational indexes for different values of SNR.

	SNR = 20 dB		SNR = 10 dB		SNR = 5 dB	
	IMSA-LS	Bare-LS	IMSA-LS	Bare-LS	IMSA-LS	Bare-LS
k_{tot}	1089	41	393	53	410	28
N	361	1089	361	1089	361	1089
f_{pos}	1.02×10^{11}	1.02×10^{11}	3.70×10^{10}	1.37×10^{11}	3.86×10^{10}	7.23×10^{10}

Although with a heavier computational burden, the choice $\gamma_{\tilde{y}^c} = \gamma_{\tilde{y}^e} = 0.01$ and $\gamma_{\tilde{L}} = 0.05$ results more effective (see figure 8(b) versus figure 8(c)).

3.2.2. Noisy data. Figures 10–12 and table 4 show the results from the comparative study carried out in correspondence with different values of signal-to-noise ratio (SNR = 20 dB, figures 10(a) versus (b); SNR = 10 dB, figures 10(c) versus (d); SNR = 5 dB, figures 10(e) versus (f)). They further confirm the reliability and efficiency of the multi-resolution strategy in terms of qualitative reconstruction errors (figure 11), especially when the noise level grows. In particular, the Bare implementation does not yield either the position or the shape of the rectangular scatterer when SNR = 5 dB, whereas the IMSA-LS properly retrieves both the barycenter and the contour of the target. As for the computational cost, it should be noticed that although the IMSA-LS requires a greater number of iterations for reaching the convergence (figure 12, table 4), the total amount of complex floating-point operations, $f_{\text{pos}} = \mathcal{O}(2 \times \eta^3) \times k_{\text{tot}}$, usually results smaller (table 4).

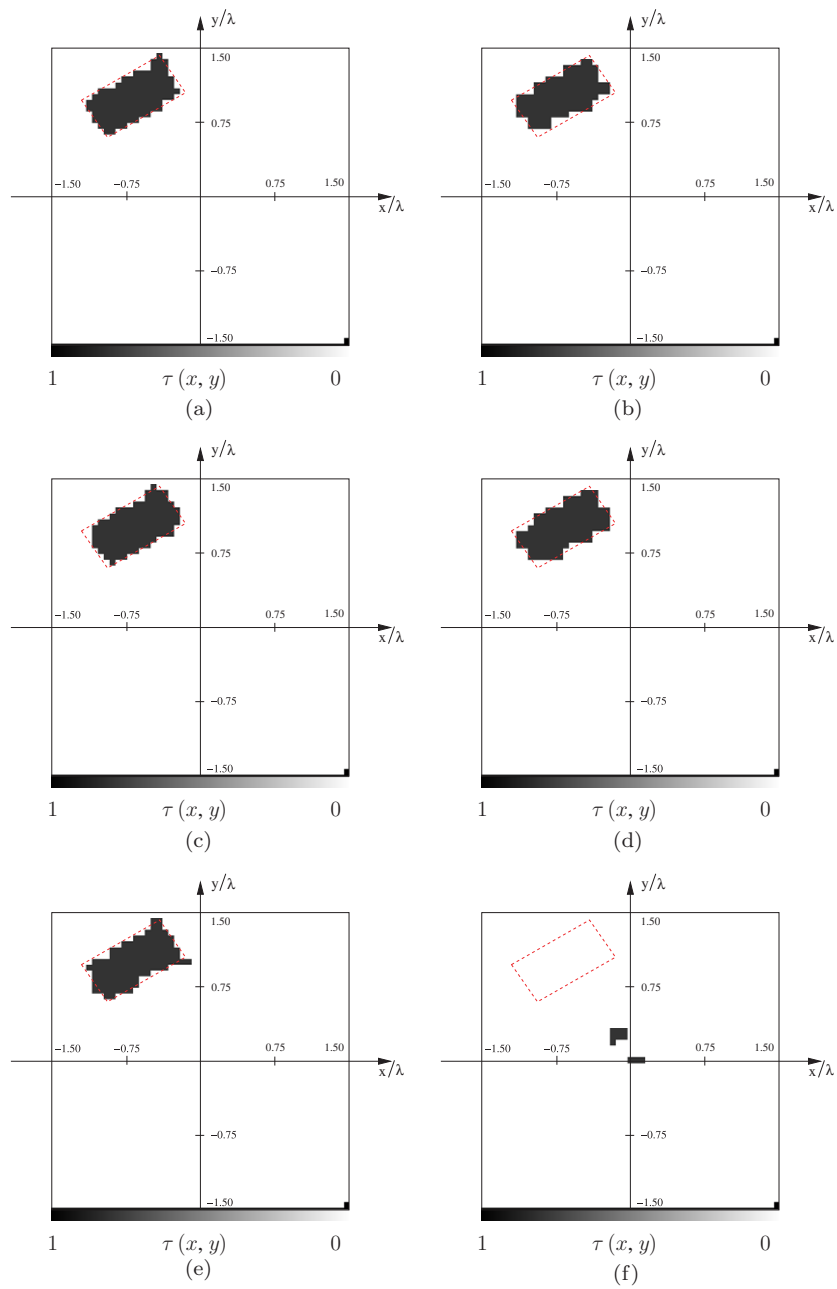


Figure 10. Numerical data. Rectangular cylinder ($\epsilon_C = 1.8$, $L_D = 3\lambda$, *noisy case*). Reconstructions with IMSA-LS (left column) and Bare-LS (right column) for different values of SNR (SNR = 20 dB (top), SNR = 10 dB (middle), SNR = 5 dB (bottom)).

3.3. Numerical data—hollow cylinder

The third test case is concerned with the inversion of the data scattered by a higher permittivity ($\epsilon_C = 2.5$) off-centered cylindrical ring, letting $L_D = 3\lambda$. The external radius of the ring is

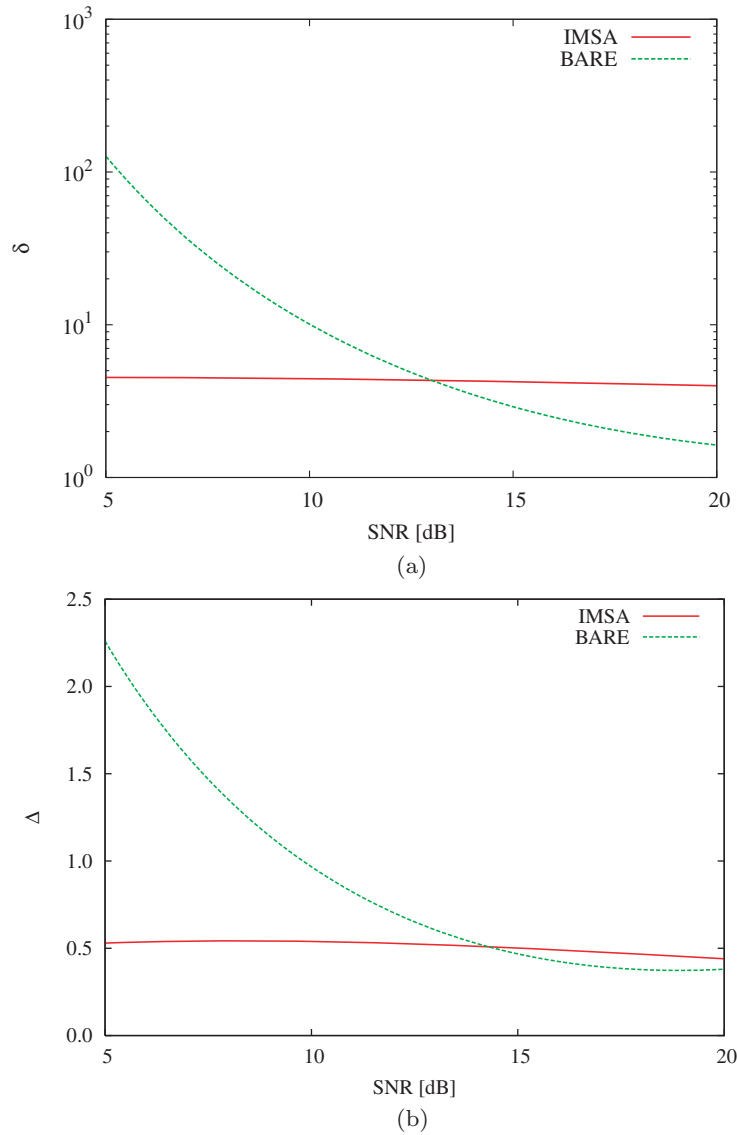


Figure 11. Numerical data. Rectangular cylinder ($\epsilon_C = 1.8$, $L_D = 3\lambda$, *noisy case*). Values of the error figures versus SNR.

$\rho_{\text{ext}} = \frac{2}{3}\lambda$, and the internal one is $\rho_{\text{int}} = \frac{\lambda}{3}$. By assuming the same arrangement of emitters and receivers as in section 3.2, the investigation domain is discretized with $N_{\text{IMSA}} = 19 \times 19$ and $N_{\text{Bare}} = 35 \times 35$ square cells for the IMSA-LS and the Bare-LS, respectively. Moreover, Δt_1 is initialized to 0.003.

As it can be observed from figure 13, where the profiles when SNR = 20 dB (figures 13(a), (b)) and SNR = 10 dB (figures 13(c), (d)) reconstructed by means of the IMSA-LS (figures 13(a), (c)) and the Bare-LS (figures 13(b), (d)) are shown, the integrated strategy usually overcomes the standard one both in locating the object and in estimating

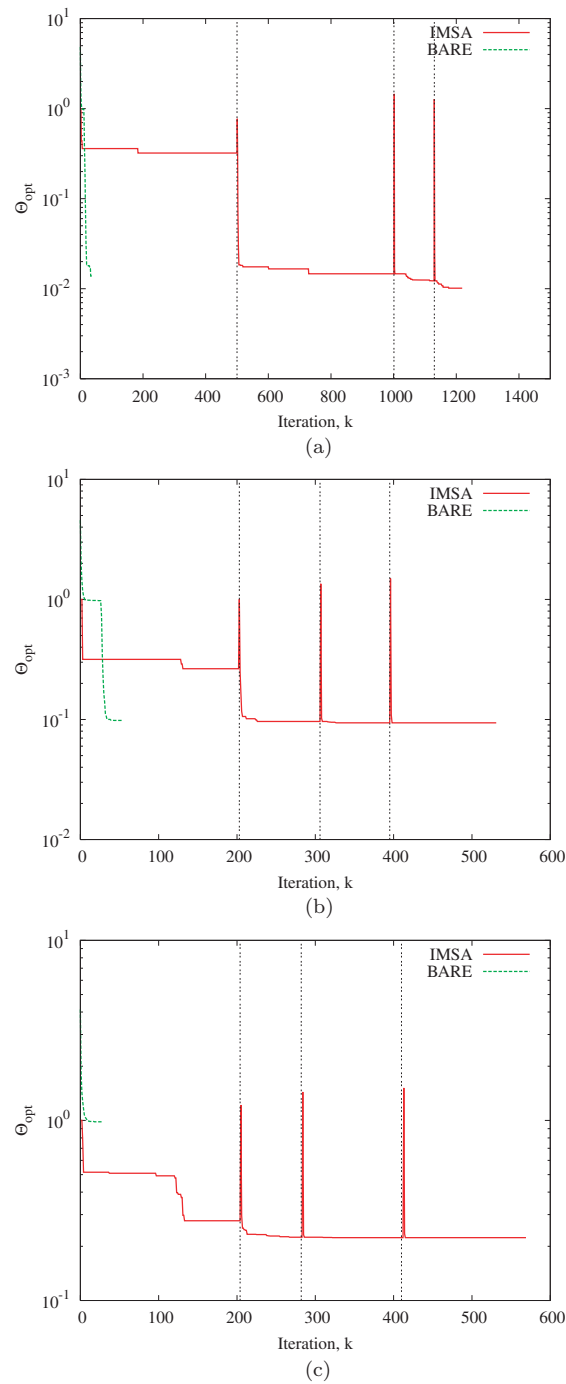


Figure 12. Numerical data. Rectangular cylinder ($\epsilon_C = 1.8$, $L_D = 3\lambda$, *noisy case*). Behavior of the cost function versus the iteration index when (a) SNR = 20 dB, (b) SNR = 10 dB and (c) SNR = 5 dB.

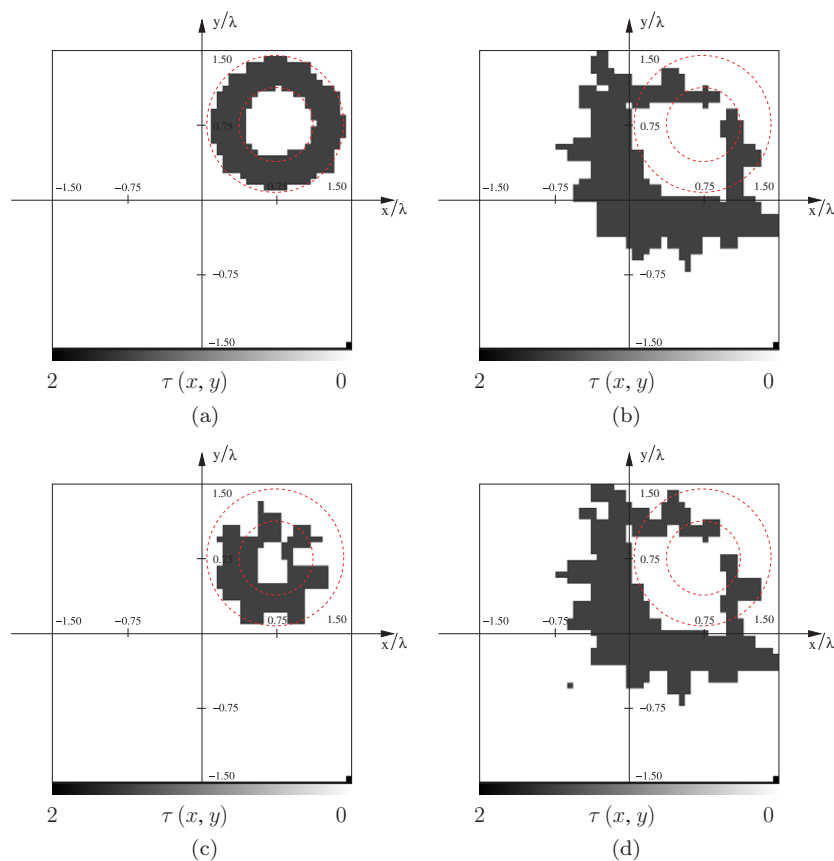


Figure 13. Numerical data. Hollow cylinder ($\epsilon_C = 2.5$, $L_D = 3\lambda$, *noisy case*). Reconstructions with IMSA-LS (left column) and Bare-LS (right column) for different values of SNR (SNR = 20 dB (top), SNR = 10 dB (bottom)).

the shape. In particular, when SNR = 20 dB, the distribution in figure 13(a) is a faithful estimate of the scatterer under test ($\delta_{\text{IMSA-LS}} = 1.25$ and $\Delta_{\text{IMSA-LS}} = 3.13$). In contrast, the reconstruction with the Bare-LS is very poor ($\delta_{\text{Bare-LS}} = 65.2$ and $\Delta_{\text{Bare-LS}} = 34.39$). Certainly, a smaller SNR value impairs the inversion as shown in figure 13(c) (compared to figure 13(a)). However, in this case, the IMSA-LS is able to properly locate the object ($\delta_{\text{IMSA-LS}} = 1.7$ versus $\delta_{\text{Bare-LS}} = 65.9$) giving rough but useful indications about its shape ($\Delta_{\text{IMSA-LS}} = 7.6$ versus $\Delta_{\text{Bare-LS}} = 34.55$).

3.4. Synthetic data—multiple scatterers

The last synthetic test case is aimed at illustrating the behavior of the IMSA-LS when dealing with $P = 3$ scatterers ($\epsilon_C = 2.0$) distanced from one another. The test geometry is characterized by an elliptic off-centered cylinder, a circular off-centered scatterer, and a square off-centered object located in a square investigation domain characterized by $L_D = 3\lambda$. By adopting the same arrangement of emitters and receivers as in section 3.3, the investigation

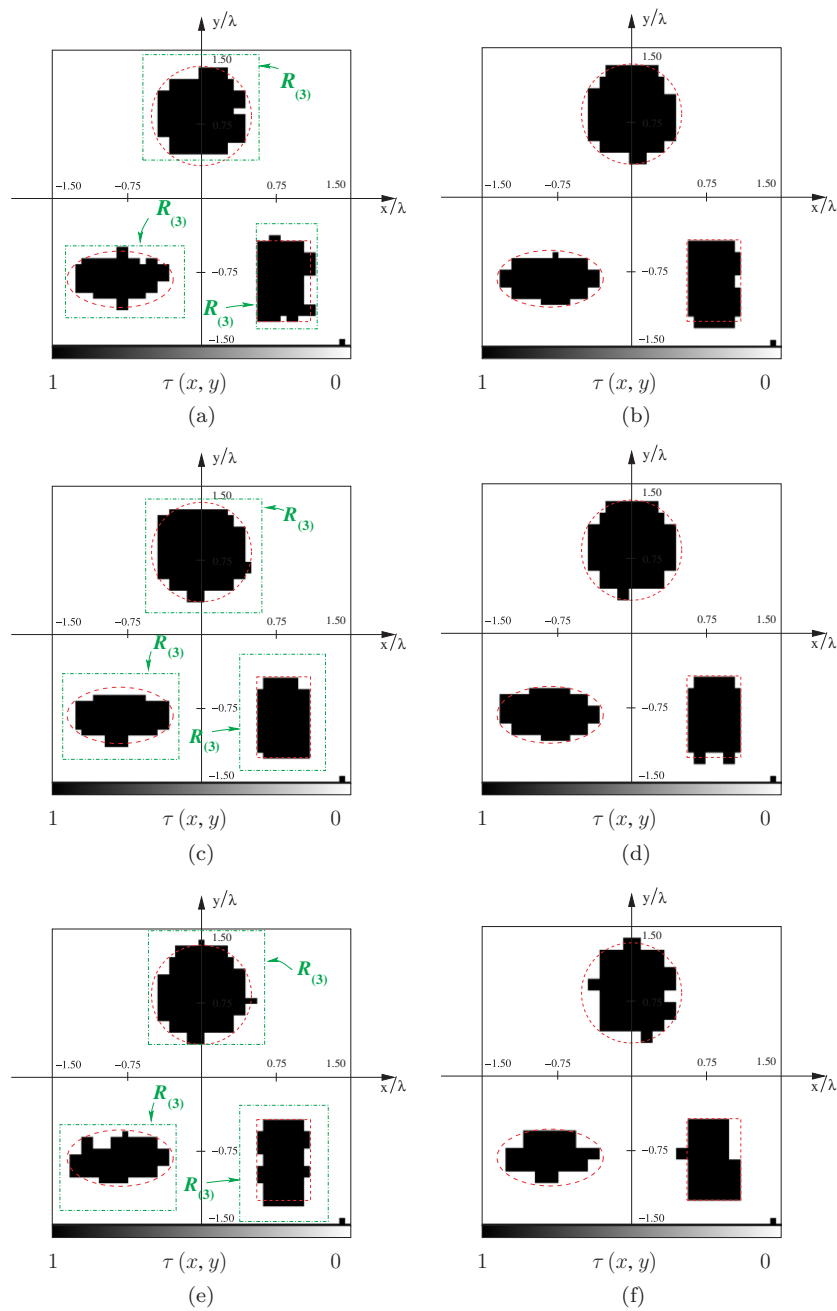


Figure 14. Numerical data. Multiple scatterers ($\epsilon_C = 2.0$, $L_D = 3\lambda$, *noisy case*). Reconstructions with IMSA-LS (left column) and Bare-LS (right column) for different values of SNR (SNR = 20 dB (top), SNR = 10 dB (middle), SNR = 5 dB (bottom)).

domain is discretized with $N_{\text{IMSA}} = 23 \times 23$ and $N_{\text{Bare}} = 31 \times 31$ square cells for the IMSA-LS and the Bare-LS, respectively. Moreover, Δt_1 is set to 0.03.

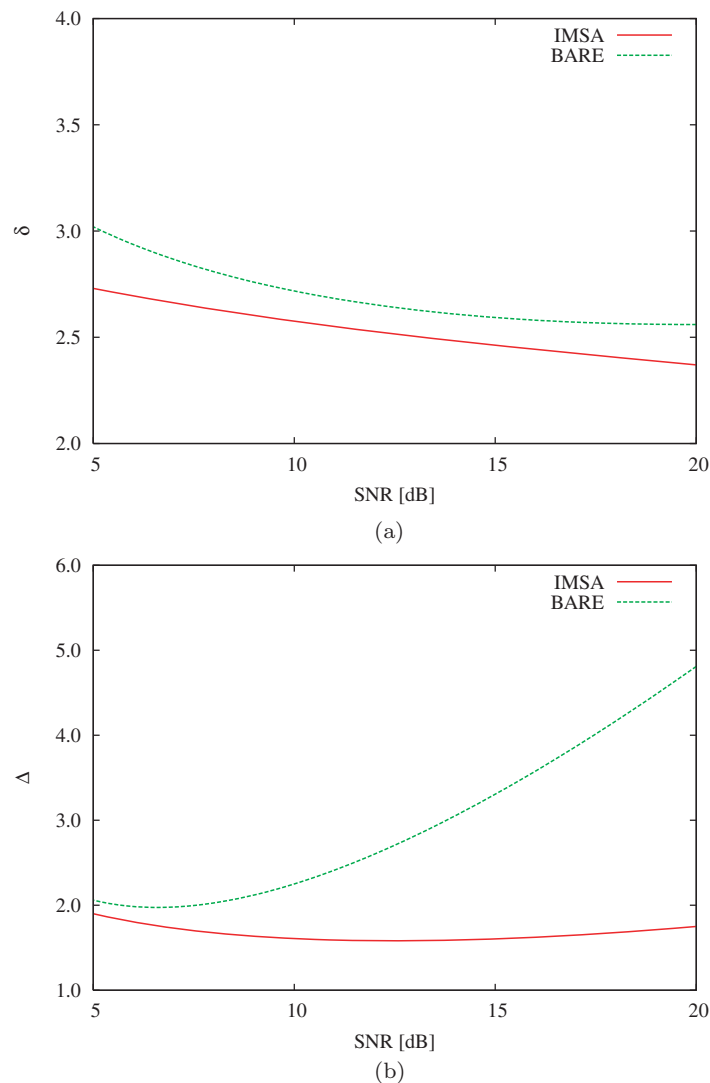


Figure 15. Multiple scatterers ($\epsilon_C = 2.0$, $L_D = 3\lambda$, *noisy case*). Values of the error figures versus SNR.

Figures 14 and 15 show the results from the comparative study carried out in correspondence with different values of signal-to-noise ratio. As shown by the reconstructions (figure 14) and as expected, the multi-resolution approach provides more accurate results and appears to be more reliable than the Bare-LS especially with low SNR. This conclusion is further confirmed by the behavior of the reconstruction errors (figure 15), for which the IMSA-LS achieves a lower localization error as well as a lower area error than those of Bare-LS, especially for SNR = 5 dB. On the other hand, both algorithms provide good estimates of the scatterer under test when inverting data affected by low noise (SNR = 20 dB, figures 14(a) versus (b); figures 15(a) and (b)).

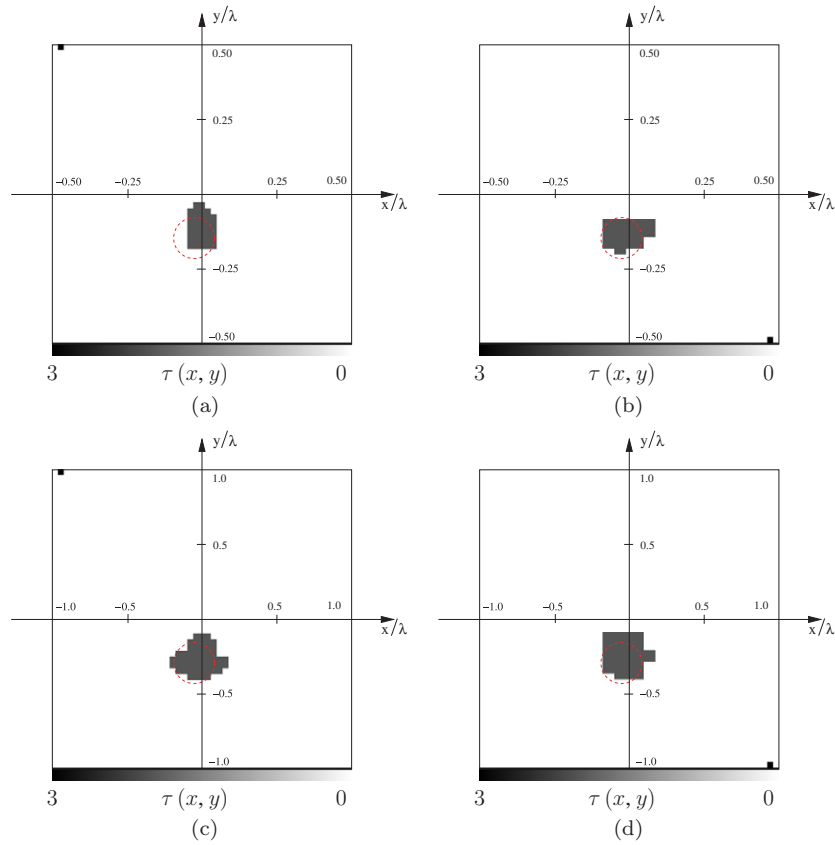


Figure 16. Experimental data (Dataset ‘Marseille’ [34]). Circular cylinder (‘dielTM_dec8f.exp’). Reconstructions with IMSA-LS (left column) and Bare-LS (right column) at different frequencies f ($f = 1$ GHz (a) and (b); $f = 2$ GHz (c) and (d) $f = 3$ GHz (e) and (f); $f = 4$ GHz (g) and (h)).

Table 5. Experimental data (Dataset ‘Marseille’ [34]). Circular cylinder (‘dielTM_dec8f.exp’). Computational indexes.

	IMSA-LS	Bare-LS	IMSA-LS	Bare-LS
	$f = 1$ GHz		$f = 2$ GHz	
k_{tot}	506	69	532	200
f_{pos}	4.88×10^9	1.22×10^{11}	5.14×10^9	3.55×10^{11}
	$f = 3$ GHz		$f = 4$ GHz	
k_{tot}	678	198	621	200
f_{pos}	6.55×10^9	3.51×10^{11}	5.99×10^9	3.55×10^{11}

3.5. Laboratory-controlled data

In order to further assess the effectiveness of the IMSA-LS also in dealing with experimental data, the multiple-frequency angular-diversity bi-static benchmark provided by *Institut Fresnel*

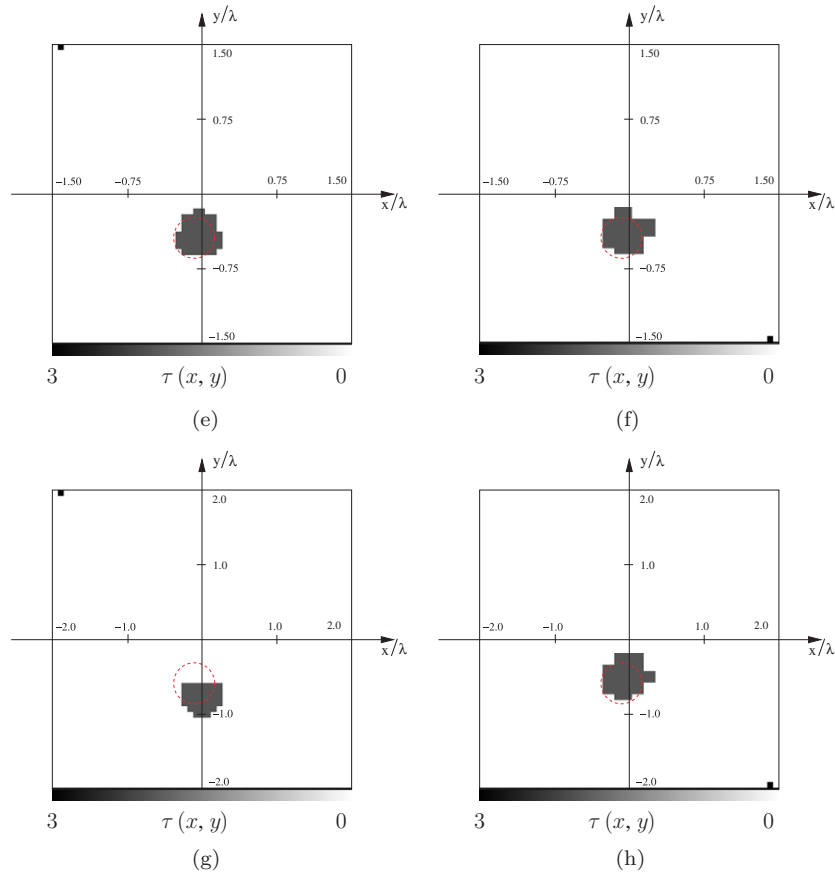


Figure 16. (Continued.)

in Marseille (France) has been considered. With reference to the experimental setup described in [34], the dataset '*dielTM_dec8f.exp*' has been processed. The field samples ($M = 49$, $V = 36$) are related to an off-centered homogeneous circular cylinder $\rho = 15$ mm in diameter, characterized by a nominal value of the object function equal to $\tau(r) = 2.0 \pm 0.3$, and located at $x_c = 0.0$, $y_c = -30$ mm within an investigation domain assumed in the following of square geometry and extension 20×20 cm². By setting $\epsilon_C = 3.0$, the reconstructions achieved are shown in figure 16 (left column) compared to those from the standard LS (right column) at $F = 4$ different operation frequencies. Whatever the frequency, the unknown scatterer is accurately localized and both algorithms yield, at convergence, structures that occupy a large subset of the true object. Such a similarity of performances, usually verified in synthetic experiments when the value of SNR is greater than 20 dB, seems to confirm the hypothesis of a low-noise environment as already evidenced in [35].

Finally, also in dealing with experimental datasets, the IMSA-LS proves its efficiency since the overall amount of complex floating point operations still remains two orders in magnitude lower than that of the Bare-LS (table 5, figure 17).

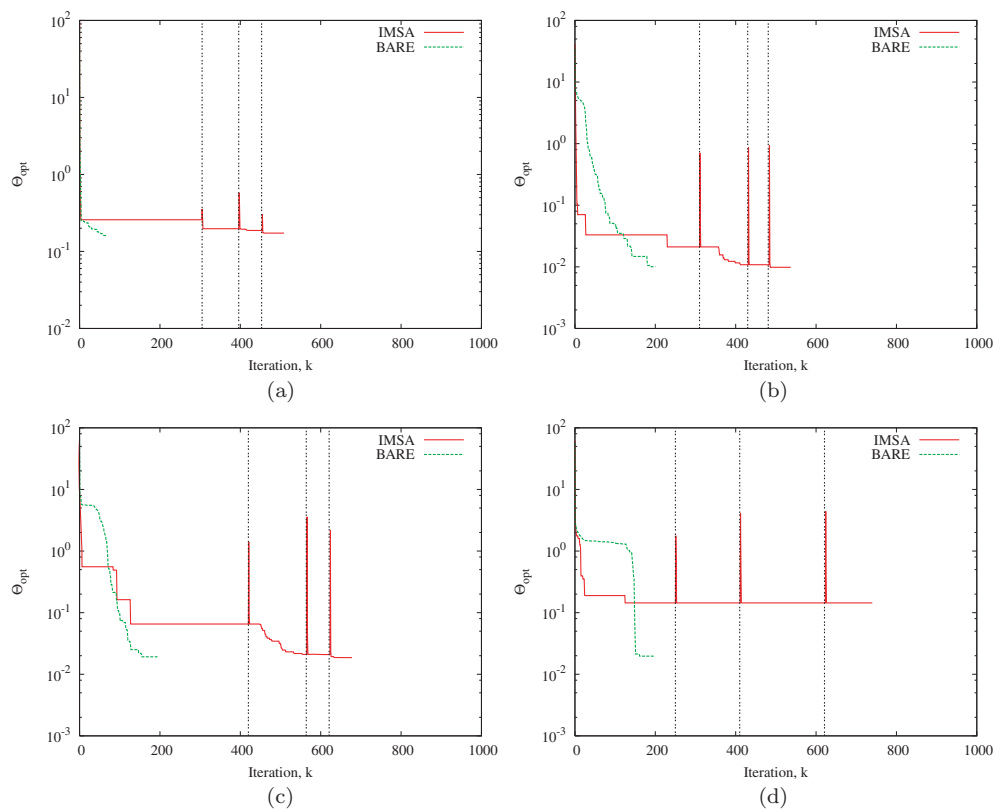


Figure 17. Experimental data (Dataset ‘Marseille’ [34]). Circular cylinder (*dieITM_dec8f.exp*). Behavior of the cost function versus the number of iterations when (a) $f = 1$ GHz, (b) $f = 2$ GHz, (c) $f = 3$ GHz and (d) $f = 4$ GHz.

4. Conclusions

In this paper, a multi-resolution approach for qualitative imaging purposes based on shape optimization has been presented. The proposed approach integrates the multi-scale strategy and the level-set representation of the problem unknowns in order to profitably exploit the amount of information collectable from the scattering experiments as well as the available *a priori* information on the scatterer under test.

The main key features of such a technique can be summarized as follows:

- innovative multi-level representation of the problem unknowns in the shape-deformation-based reconstruction technique;
- effective exploitation of the scattering data through the iterative multi-step strategy;
- limitation of the risk of being trapped in false solutions thanks to the reduced ratio between data and unknowns;
- useful exploitation of the *a priori* information (i.e., object homogeneity) about the scenario under test;
- enhanced spatial resolution limited to the region of interest.

From the validation concerned with different scenarios and both synthetic and experimental data, the following conclusions can be drawn:

- the IMSA-LS usually proved more effective than the single-resolution implementation, especially when dealing with corrupted data scattered from simple as well as complex geometries characterized by one or several objects;
- the integrated strategy appeared less computationally expensive than the standard approach in reaching a reconstruction with the same level of spatial resolution within the support of the object.

References

- [1] Shull P J 2002 *Nondestructive Evaluation: Theory, Techniques and Applications* (Boca Raton, FL: CRC Press)
- [2] Baruchel J, Buffière J-Y, Maire E, Merle P and Peix G 2000 *X-Ray Tomography in Material Science* (Paris: Hermes Science)
- [3] Schmerr L W 1998 *Fundamentals of Ultrasonic Nondestructive Evaluation: A Modeling Approach* (Berlin: Springer)
- [4] Auld B A and Moulder J C 1999 Review of advances in quantitative eddy current nondestructive evaluation *J. Nondestruct. Eval.* **18** 3–36
- [5] Zoughi R 2000 *Microwave Nondestructive Testing and Evaluation* (Dordrecht: Kluwer)
- [6] Bucci O M and Isernia T 1997 Electromagnetic inverse scattering: retrievable information and measurement strategies *Radio Sci.* **32** 2123–38
- [7] Bertero M and Boccacci P 1998 *Introduction to Inverse Problems in Imaging* (Bristol: Institute of Physics Publishing)
- [8] Bucci O M and Franceschetti G 1987 On the spatial bandwidth of scattered fields *IEEE Trans. Antennas Propagat.* **35** 1445–55
- [9] Isernia T, Pascazio V and Pierri R 2001 On the local minima in a tomographic imaging technique *IEEE Trans. Antennas Propagat.* **39** 1696–07
- [10] Haddar H, Kusiak S and Sylvester J 2005 The convex back-scattering support *SIAM J. Appl. Math.* **66** 591–615
- [11] Miller E L and Willsky A S 1996 A multiscale, statistically based inversion scheme for linearized inverse scattering problems *IEEE Trans. Antennas Propagat.* **34** 346–57
- [12] Baussard A, Miller E L and Lesselier D 2004 Adaptive multiscale reconstruction of buried objects *Inverse Problems* **20** S1–S15
- [13] Li J, Liu H and Zou J 2008 Multilevel linear sampling method for inverse scattering problems *SIAM J. Appl. Math.* **30** 1228–50
- [14] Caorsi S, Donelli M and Massa A 2004 Detection, location, and imaging of multiple scatterers by means of the iterative multiscaling method *IEEE Trans. Microwave Theory Tech.* **52** 1217–28
- [15] Caorsi S, Massa A, Pastorino M and Donelli M 2004 Improved microwave imaging procedure for nondestructive evaluations of two-dimensional structures *IEEE Trans. Antennas Propagat.* **52** 1386–97
- [16] Benedetti M, Donelli M and Massa A 2007 Multicrack detection in two-dimensional structures by means of GA-based strategies *IEEE Trans. Antennas Propagat.* **55** 205–15
- [17] Cingoski V, Kowata N, Kaneda K and Yamashita H 1999 Inverse shape optimization using dynamically adjustable genetic algorithms *IEEE Trans. Energy Convers.* **14** 661–6
- [18] Lizzi L, Viani F, Azaro R and Massa A 2007 Optimization of a spline-shaped UWB antenna by PSO *IEEE Antennas Wireless Propagat. Lett.* **6** 182–5
- [19] Cea J, Garreau S, Guillaume P and Masmoudi M 2000 The shape and topological optimizations connection *Comput. Methods Appl. Mech. Eng.* **188** 713–26
- [20] Feijoo G R, Oberai A A and Pinsky P M 2004 An application of shape optimization in the solution of inverse acoustic scattering problems *Inverse Problems* **20** 199–228
- [21] Masmoudi M, Pommier J and Samet B 2005 The topological asymptotic expansion for the Maxwell equations and some applications *Inverse Problems* **21** 547–64
- [22] Santosa F 1996 A level-set approach for inverse problems involving obstacles *ESAIM: COCV* **1** 17–33
- [23] Litman A, Lesselier D and Santosa F 1998 Reconstruction of a two-dimensional binary obstacle by controlled evolution of a level-set *Inverse Problems* **14** 685–706
- [24] Dorn O, Miller E L and Rappaport C M 2000 A shape reconstruction method for electromagnetic tomography using adjoint fields and level sets *Inverse Problems* **16** 1119–56
- [25] Ramananjaona C, Lambert M, Lesselier D and Zolésio J P 2001 Shape reconstruction of buried obstacles by controlled evolution of a level-set: from a min–max formulation to a numerical experimentation *Inverse Problems* **17** 1087–111

- [26] Ferrayé R, Dauvignac J-Y and Pichot C 2003 An inverse scattering method based on contour deformations by means of a level set method using frequency hopping technique *IEEE Trans. Antennas Propagat.* **51** 1100–13
- [27] Chung E T, Chan T F and Tai X C 2005 Electrical impedance tomography using level set representation and total variational regularization *J. Comput. Phys.* **205** 707–23
- [28] van den Doel K and Asher U M 2007 Dynamic level set regularization for large distributed parameter estimation problems *Inverse Problems* **23** 1271–88
- [29] Strain J 1999 Three methods for moving interfaces *J. Comput. Phys.* **151** 616–48
- [30] Dorn O and Lesselier D 2006 Level set methods for inverse scattering *Inverse Problems* **22** R67–131
- [31] Richmond J H 1965 Scattering by a dielectric cylinder of arbitrary cross-section shape *IEEE Trans. Antennas Propagat.* **13** 334–41
- [32] Osher S and Sethian J A 1988 Fronts propagating with curvature-dependent speed: algorithms based on Hamilton–Jacobi formulations *J. Comput. Phys.* **79** 12–49
- [33] Sethian J A 1999 *Level Set and Fast Marching Methods* 2nd edn (Cambridge: Cambridge University Press)
- [34] Belkebir K and Saillard M 2001 Testing inversion algorithms against experimental data *Inverse Problems* **17** 1565–702
- [35] Testorf M and Fiddy M 2001 Imaging from real scattered field data using a linear spectral estimation technique *Inverse Problems* **17** 1645–58